ResearchGate

See discussions, stats, and author profiles for this publication at: https://www.researchgate.net/publication/348438176

Force-based finite element formulation for nonlinear behaviour of reinforced concrete frames

Article *in* Innovative Infrastructure Solutions · June 2021

DOI: 10.1007/s41062-020-00413-9

CITATIONS
3

READS
185

2 authors:

Sameera Hippola
University of Liège
11 PUBLICATIONS **69** CITATIONS
SEE PROFILE

Kushan Wijesundara
University of Peradeniya
108 PUBLICATIONS **793** CITATIONS
SEE PROFILE

All content following this page was uploaded by Sameera Hippola on 31 March 2021.

The user has requested enhancement of the downloaded file.

Author's personal copy

Innovative Infrastructure Solutions (2021) 6:48
https://doi.org/10.1007/s41062-020-00413-9

TECHNICAL PAPER

Force-based finite element formulation for nonlinear behaviour of reinforced concrete frames

H. M. S. S. Hippola[1] · **K. K. Wijesundara**[1]

Received: 22 September 2020 / Accepted: 19 November 2020
© Springer Nature Switzerland AG 2021

Abstract

This paper presents a nonlinear force-based finite element formulation which can predict the behaviour of reinforced concrete frames, explicitly satisfying section-level equilibrium. In the existing nonlinear force-based fibre beam–column element formulation, two nested iterative procedures are utilized at the structure and element levels. In the element-level iterative procedure, the strain states of the fibre level are iteratively altered by following the corrective forces suggested by the element level. When this algorithm is implemented with uniaxial material models, the element residual deformations can be minimized effectively by altering the axial strains, which is the only variable at the fibre level, implicitly achieving the section-level equilibrium to a reasonable accuracy. However, when a cracked reinforced concrete constitutive model, which accounts for axial–flexure–shear interaction, is implemented, element-level convergence becomes problematic because element residual deformations have to be minimized by altering all three strain components with additional constraints at the fibre level. To address this issue, this paper proposes a novel force-based finite element formulation by implementing an iterative procedure at the section level in order to minimize section unbalanced forces at section level itself, rather than transferring errors of the section level to element level. The current study focuses to test this algorithm for only axial force–bending moment interaction response. The proposed formulation was experimentally validated and was proved to be stable and accurate to predict the nonlinear responses of RC frames.

Keywords RC frames · Nonlinear static analysis · Force-based fibre beam–column element · Axial force–bending moment interaction · Section-level equilibrium

Introduction

To assess the structural performance of reinforced concrete (RC) frames under severe earthquakes and winds, it is vital to model and simulate the nonlinear behaviour accounting the geometric and material nonlinearities [1].

In general, there are three types of models that can be used to simulate the nonlinear behaviour of RC frames, namely lumped plasticity models [2–5], distributed plasticity models [6, 7] and 3-dimensional continuum finite element models [8–10]. Out of these models, distributed plasticity models provide a good compromise between the accuracy of results and the computational effort required [11]. The plasticity is monitored along each line element in the distributed plasticity model with the aid of control stations or integration points. In such elements, the relationship between element nodal deformation and nodal force increments can be derived using force-based, displacement-based [12–15] or mixed finite element formulations [16, 17]. In the displacement-based formulation, equilibrium is satisfied in weak form while compatibility and constitutive relationship are satisfied in strong form. In the force-based finite element formulation, as the exact internal force variation in the line element is known through force shape functions, it does not require element discretization in order to accurately capture the nonlinear response [18, 19]. Therefore, force-based finite elements are popular among researchers over displacement-based finite elements when modelling RC frames, owing to the drastic reduction in number of degrees of freedom in force-based frame models without sacrificing the accuracy and the stability.

✉ K. K. Wijesundara
kushanw@pdn.ac.lk

H. M. S. S. Hippola
sameerahippola@eng.pdn.ac.lk

[1] Department of Civil Engineering, University of Peradeniya, Peradeniya, Sri Lanka

Published online: 12 January 2021

Author's personal copy

Force-based finite element formulation was first implemented in a line element [20] by interpolating both section deformations and section flexibilities to account axial force–bending moment interaction. Subsequently, a new force-based fibre element was introduced considering the force dependent interpolation functions that are updated during the analysis [21], and it was later improved by Zeris and Mahin [22–24]. However, these proposed formulations failed to be integrated into a general-purpose finite element program due to the violation of initial equilibrium assumption. In addition, it was difficult to calculate element resisting forces corresponding to a given element nodal deformation. To overcome these problems, Ciampi and Carlesimo [25] introduced a consistent force-based method, which was later refined to formulate the force-based fibre beam–column element [26, 27]. The application of this formulation to predict nonlinear hysteresis behaviour of reinforced concrete beam specimens can be found in many studies available in the literature [28]. Later, efforts were devoted to include effects of bond slip [29, 30], effects of large displacements [31, 32] to the fibre beam–column element and solve localization issues [33].

In the existing force-based fibre beam–column element formulation, equilibrium, compatibility and constitutive relationships are satisfied at structure level, element level and fibre level, respectively. It has two nested iterative procedures at structure level and element level. The element-level iterative procedure ultimately computes the element resisting forces corresponding to a given element deformation increment by minimizing the element residual deformations through a series of corrective element forces computed at the element level. This algorithm is stable and accurately captures axial force–bending moment interaction (N-M interaction) of RC frames when implemented with uniaxial material models at fibre level. However, the indirect minimization of section unbalanced forces through element corrective forces becomes problematic and the element-level iteration fails to converge the element forces when more advanced constitutive models are used at fibre level, especially to capture complete axial force–bending moment–shear force interaction (N–M–V interaction) [34]. It was evident that in such cases, the section unbalanced forces should be explicitly treated rather than implicitly minimized through corrective forces computed at element level. To address this issue, the current study focuses to alter the existing formulation by employing an iterative procedure at section level rather than at element level. The main advantage of this alteration is that the section-level iterative procedure explicitly minimizes the section unbalanced forces at section level itself, without transferring them to element level. Furthermore, it allows to compute updated section deformation and updated tangent section stiffness matrix for a given section force increment. Accordingly, a complete nonlinear force-based algorithm was developed to capture N–M interaction. The authors believe that the proposed formulation enriches the existing force-based fibre beam–column element formulation, potentially opening doors towards addressing section specific phenomenon such as capturing the N–M–V interaction that has proved difficult to capture through the existing force-based fibre beam–column element formulation.

Proposed formulation

The proposed novel formulation is based on state determination processes at structure level, element level, section level and fibre level. There are two nested iterative procedures at structure level and section level. The formulation was written using displacement control method where displacement is applied in series of steps to a specific degree of freedom of the structure. By completing state determination processes at all hierarchical levels for a certain displacement step, structure force increment and deformation increment corresponding to the applied displacement step can be computed. The state determination procedures are explained in the following sections. The algorithm was developed to perform nonlinear static analysis of planar frames.

Structure state determination

In displacement control method of structure state determination, an iterative procedure is used to calculate the structure nodal force and nodal displacement increment vectors corresponding to the displacement increment ΔU_2 applied at a specific degree of freedom.

In the equations given in this section, the structure nodal force increment vector $\{\Delta F\}$, nodal displacement increment vector $\{\Delta U\}$ and structure tangent stiffness matrix $[K]$ are given in condensed format in Eqs. (1), (2) and (3), respectively, as the incremental structure equilibrium equations are solved using static condensation method.

$$\{\Delta F\} = \begin{Bmatrix} \Delta F_1 \\ \Delta F_2 \end{Bmatrix} = \Delta\lambda \begin{Bmatrix} P_1 \\ P_2 \end{Bmatrix} \tag{1}$$

$$\{\Delta U\} = \begin{Bmatrix} \Delta U_1 \\ \Delta U_2 \end{Bmatrix} \tag{2}$$

$$[K] = \begin{bmatrix} K_{11} & K_{12} \\ K_{21} & K_{22} \end{bmatrix} \tag{3}$$

In Eq. (1), ΔF_2 denotes the force increment at the specific degree of freedom where the displacement increment is applied and $\{\Delta F_1\}$ is a known vector after reaction force components are left out by applying boundary conditions.

Author's personal copy

Furthermore, $\{\Delta F\}$ can be expressed as load factor increment $\Delta\lambda$ times a vector $\begin{Bmatrix} P_1 \\ P_2 \end{Bmatrix}$ where $\{P_1\}$ is a known vector and P_2 denotes unity. In Eq. (2), ΔU_2 represents the nodal displacement increment applied to the specific degree of freedom and $\{\Delta U_1\}$ represents the nodal displacement increment vector of other degrees of freedom excluding the nodal displacements of the restrained degrees of freedom.

In the first structure-level iteration ($i = 1$), the structure tangent stiffness matrix of the previous displacement increment $[K]_{i=0}$ is used to calculate the initial estimation of the load factor increment $\Delta\lambda_{i=1}$ and the nodal displacement increment vector $\{\Delta U\}_{i=1}$ for a given nodal displacement increment ΔU_2 as follows.

$$\{\Delta U\}_{i=1} = \begin{Bmatrix} \Delta U_1 \\ \Delta U_2 \end{Bmatrix}_{i=1} = [K]^{-1}_{i=0}\Delta\lambda_{i=1}\begin{Bmatrix} P_1 \\ P_2 \end{Bmatrix} \tag{4}$$

The solution of this incremental equilibrium equation ($\Delta\lambda_{i=1}$ and $\{\Delta U\}_{i=1}$) is schematically shown by lines AA' in Fig. 1a and b for the displacement controlling node and other displacement components, respectively. The gradient of AA' represents $[K]_{i=0}$.

Once $\{\Delta U\}_{i=1}$ is calculated, the element state determination process (in Sect. 2.2) can be carried out to compute updated element tangent stiffness matrices and structure updated tangent stiffness matrix $[K]_{i=1}$. Subsequently, the incremental structure nodal resisting force vector $\begin{Bmatrix} R_1 \\ R_2 \end{Bmatrix}_{i=1}$ can be calculated as given in Eq. (5)

$$\begin{Bmatrix} R_1 \\ R_2 \end{Bmatrix}_{i=1} = [K]_{i=1}\begin{Bmatrix} \Delta U_1 \\ \Delta U_2 \end{Bmatrix}_{i=1} \tag{5}$$

where R_2 represents the resisting force at the degree of freedom where the displacement increment is applied, and $\{R_1\}$ denotes nodal resisting force vector of the other degrees of freedom excluding the values at restrained degrees of freedom. The components $R_{2,i=1}$ and $\{R_1\}_{i=1}$ computed employing $[K]_{i=1}$ in Eq. (5) are illustrated in Fig. 1a and b, respectively. The nodal unbalanced force vector $\begin{Bmatrix} O_1 \\ O_2 \end{Bmatrix}_{i=1}$ can be then calculated as given in Eq. (6).

$$\begin{Bmatrix} O_1 \\ O_2 \end{Bmatrix}_{i=1} = \begin{Bmatrix} O_1 \\ O_2 \end{Bmatrix}_{i-1} + \Delta\lambda_{i=1}\begin{Bmatrix} P_1 \\ P_2 \end{Bmatrix} - \begin{Bmatrix} R_1 \\ R_2 \end{Bmatrix}_{i=1} \tag{6}$$

where $\begin{Bmatrix} O_1 \\ O_2 \end{Bmatrix}_{i-1}$ is the nodal unbalanced force vector of the previous structure-level iteration ($i-1$) and it is taken as a null vector for the first structure-level iteration ($i = 1$) of each displacement increment, O_2 represents the unbalanced force at the degree of freedom where the displacement increment is applied, and $\{O_1\}$ denotes the nodal unbalanced force vector of other degrees of freedom excluding the values at the restrained degrees of freedom. The components $O_{2,i=1}$ and $\{O_1\}_{i=1}$ computed in Eq. (6) are illustrated in Fig. 1a and b, respectively. If $\begin{Bmatrix} O_1 \\ O_2 \end{Bmatrix}_{i=1}$ is not within the tolerance, the algorithm will proceed into the second structure-level iteration ($i = 2$) to compute a corrective load factor increment $\Delta\lambda_{i=2}$ and a nodal displacement increment $\begin{Bmatrix} \Delta U_1 \\ \Delta U_2 \end{Bmatrix}_{i=2}$ linearizing around $[K]_{i=1}$ as given in Eq. (7).

$$\begin{Bmatrix} \Delta U_1 \\ \Delta U_2 \end{Bmatrix}_{i=2} = [K]^{-1}_{i=1}\begin{Bmatrix} O_1 \\ O_2 \end{Bmatrix}_{i=1} + [K]^{-1}_{i=1}\Delta\lambda_{i=2}\begin{Bmatrix} P_1 \\ P_2 \end{Bmatrix} \tag{7}$$

The constraint to solve Eq. (7) is to maintain the initially applied displacement increment $\Delta U_{2,i=1}$ at the displacement controlling degree of freedom as a constant; thus, $\Delta U_{2,i}$ should be zero in the second and subsequent structure-level iterations (when $i > 1$). The first component in Eq. (7), $[K]^{-1}_{i=1}\begin{Bmatrix} O_1 \\ O_2 \end{Bmatrix}_{i=1}$ introduces a value to $\Delta U_{2,i=2}$ which violates the constraint of solving Eq. (7) and is represented by the line BB' in Fig. 2a. However, $\Delta\lambda_{i=2}$ in the second component of Eq. (7) will be computed such that the resultant $\Delta U_{2,i=2}$ in Eq. (7) should be zero. This

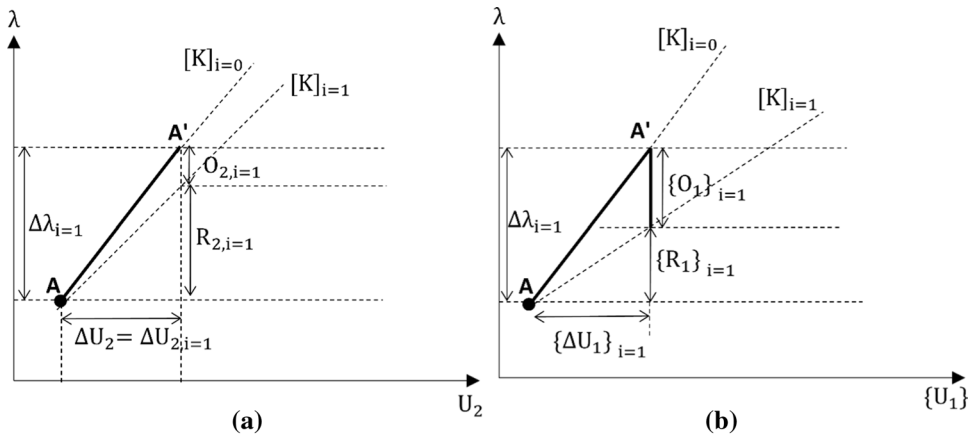

Fig. 1 Schematic diagram of the first structure-level iteration: **a** at the displacement controlling node and **b** at other DOFs excluding restrained DOFs

Author's personal copy

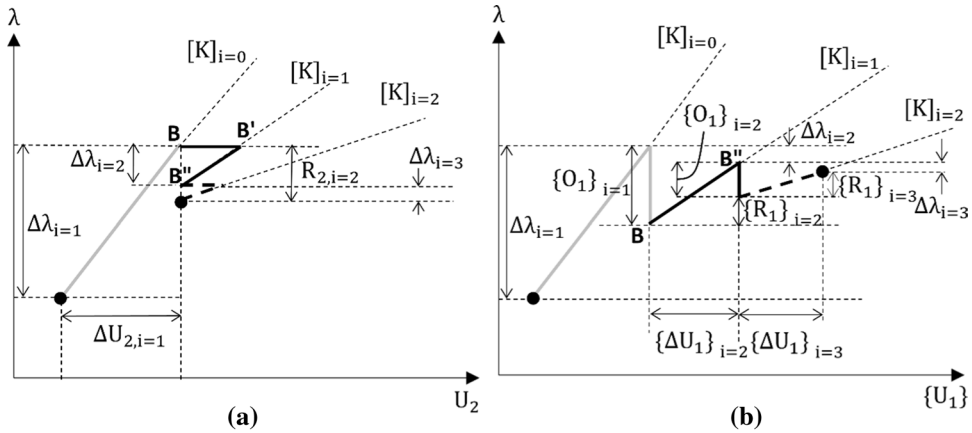

Fig. 2 Schematic diagram of the subsequent structure-level iterations of structure state determination: **a** at the displacement controlling node and **b** at other DOFs excluding restrained DOFs

operation is represented by line $B'B''$ in Fig. 2a. In general, Eq. (7) corrects the nodal unbalanced force at $i = 1$ linearizing around $[K]_{i=1}$, maintaining the displacement increment applied at the controlling degree of freedom constant. The points BB'' in Fig. 2a and b represent the complete operation of Eq. (7), where $\Delta U_{2,i=2}$ is held at zero and a change in other nodal displacements $\{\Delta U\}_{i=1}$ is present.

Subsequently, element state determination can be performed again to find the updated structure tangent stiffness matrix $[K]_{i=2}$. Then, structure nodal resisting force vector $\begin{Bmatrix} R_1 \\ R_2 \\ O_1 \\ O_2 \end{Bmatrix}_{i=2}$ and structure nodal unbalanced force vector $\begin{Bmatrix} O_1 \\ O_2 \end{Bmatrix}_{i=2}$ can be computed as previously given in Eqs. (5) and (6). Schematic representations of these computations are illustrated in Fig. 2a and b.

This procedure is continued as shown in dotted lines of Fig. 2a and b until the nodal unbalanced force vector $\begin{Bmatrix} O_1 \\ O_2 \end{Bmatrix}_i$ becomes less than a prescribed tolerance and yields the correct structure nodal force increment and nodal displacement increment corresponding to the applied displacement step ΔU_2.

Element state determination

The element state determination process is specifically designed to compute updated element stiffness matrix $[K^e]_i$ of each element in the structure at ith structure-level iteration.

At the beginning of the element state determination process, element nodal displacement increment vector $\{\Delta q_{\text{global}}\}_i$ extracted from the structure nodal displacement increment vector $\{\Delta U\}_i$ is transformed from global co-ordinate system to the local co-ordinate system using the rotational transformation matrix $[\Gamma_{\text{ROT}}]$ as given in Eq. (8).

$$\{\Delta q_{\text{local}}\}_i = [\Gamma_{\text{ROT}}]\{\Delta q_{\text{global}}\}_i \tag{8}$$

Rigid body modes are then removed from the element nodal displacement increment vector $\{\Delta q_{\text{local}}\}_i$ using rigid body transformation matrix $[\Gamma_{\text{RBM}}]$ to obtain element nodal displacement increment vector $\{\Delta q\}_i$ in the basic system as given in Eq. (9).

$$\{\Delta q\}_i = [\Gamma_{\text{RBM}}]\{\Delta q_{\text{local}}\}_i \tag{9}$$

The components of nodal force and nodal displacement increment vectors $\{\Delta Q\}_i$ and $\{\Delta q\}_i$ of the basic system are illustrated in Fig. 3.

Once $\{\Delta q\}_i$ is known, the element nodal force increment vector $\{\Delta Q_i\}$ can be calculated using the element stiffness matrix of the previous iteration $[K^e]_{i-1}$ as given in Eq. (10).

$$\{\Delta Q\}_i = [K^e]_{i-1}\{\Delta q\}_i - \{\Delta Q_{\text{unb}}\}_{i-1} \tag{10}$$

where $\{\Delta Q_{\text{unb}}\}_{i-1}$ refers to the element nodal unbalanced force vector of the previous structure-level iteration (calculated as given in Eq. (12)) and is taken as a null vector at the first structure-level iteration ($i = 1$) for each displacement increment. The computation given in Eq. (10) is schematically represented in Fig. 4 by the paths CC', $C'DD'$ and $D'EE'$ for the 1st, 2nd and 3rd structure-level iterations, respectively.

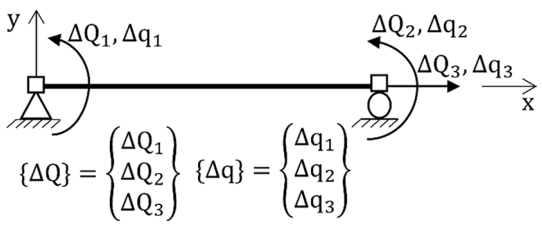

Fig. 3 Nodal forces and deformations of the basic system referring local co-ordinate system (x, y)

Author's personal copy

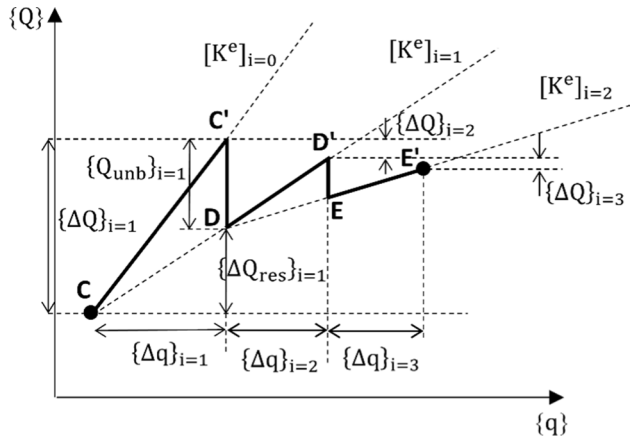

Fig. 4 Schematic diagram of element state determination

The points C, C', D' and E' represent the deformation states and force states of the basic system with the progression of structure-level iterations. Once the element nodal force increment vector $\{\Delta Q\}_i$ is computed for a particular element, the section state determination process (in Sect. 2.3) can be carried out for all the sections of the element to obtain the updated element tangent stiffness matrix $[K^e]_i$. Figure 5 illustrates the integration points where the fibre sections are assigned to carry out section state determination in an element and how fibre sections are discretized at each integration point.

The updated element tangent stiffness matrix $[K^e]_i$ can be used to compute element resisting force vector $\{\Delta Q_{\text{res}}\}_i$ corresponding to the element displacement increment vector $\{\Delta q\}_i$ as given in Eq. (11).

$$\{\Delta Q_{\text{res}}\}_i = [K^e]_i \{\Delta q\}_i \tag{11}$$

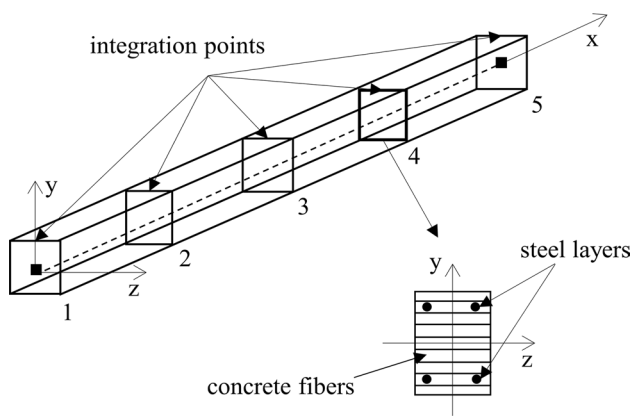

Fig. 5 Integration points and division of a section into fibres of the force-based frame element without rigid body modes

The element unbalanced force vector $\{\Delta Q_{\text{unb}}\}_i$ which is required to compute $\{\Delta Q\}_{i+1}$ in the next structure-level iteration is computed as given in Eq. (12).

$$\{\Delta Q_{\text{unb}}\}_i = [K^e]_{i-1} \{\Delta q\}_i - \{\Delta Q_{\text{res}}\}_i \tag{12}$$

Figure 4 schematically represents $\{\Delta Q_{res}\}_i$ and $\{\Delta Q_{unb}\}_i$ for the first structure-level iteration. Subsequently, by introducing rigid body modes and transforming the co-ordinate system to the global co-ordinate system, the updated element stiffness matrix in global co-ordinate system $[K^e_{\text{global}}]_i$ can be obtained as in Eq. (13).

$$\left[K^e_{\text{global}}\right]_i = [\tau_{\text{ROT}}]^T \left([\tau_{\text{RBM}}]^T [K^e]_i [\tau_{\text{RBM}}] \right) [\tau_{\text{ROT}}] \tag{13}$$

By assembling $\left[K^e_{\text{global}}\right]_i$ of all the elements, updated structure stiffness matrix $[K]_i$ can be computed. It is important to note that in this formulation, no iteration is carried out at the element level.

Section state determination

The section state determination is specifically designed to generate the updated section tangent stiffness matrix and updated section deformation vector for a given section force increment vector $\{\Delta S\}_i$ at ith structure-level iteration. This is achieved through employing an iterative procedure at the section level to explicitly minimize the section unbalanced forces, as illustrated in Fig. 6.

The section force increment vector $\{\Delta S\}_i$ at the ith structure-level iteration and section force $\{S\}_i$ of each section of a particular element can be calculated using corresponding element nodal force increment vector $\{\Delta Q\}_i$ and force interpolation function matrix $\left[N^h\right]$ as given in Eqs. (14) and (15).

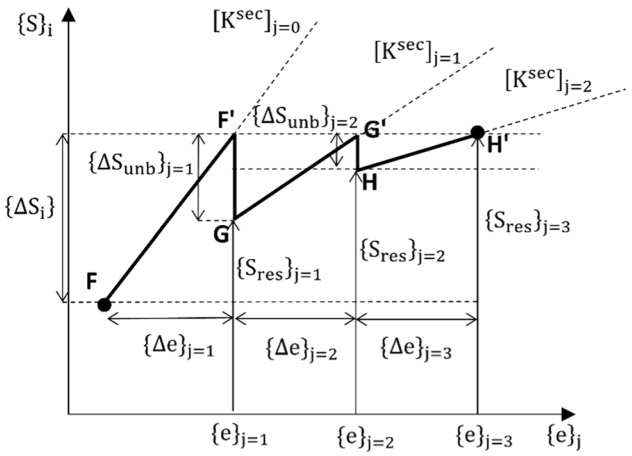

Fig. 6 Schematic diagram of section state determination

Author's personal copy

$$\{\Delta S\}_i = \left[N^h\right]\{\Delta Q\}_i \tag{14}$$

$$\{S\}_i = \{S\}_{i-1} + \{\Delta S\}_i \tag{15}$$

Figure 7 illustrates the components of section force and deformation vectors.

In the first section-level iteration ($j = 1$), the estimation of the section deformation increment vector $\{\Delta e\}_{j=1}$ is initially computed linearizing around the section tangent stiffness matrix of the previous iteration $[K^{\text{sec}}]_{j=0}$ as given in Eq. (16). This computation is schematically represented by line FF′ in Fig. 6.

$$\{\Delta e\}_{j=1} = \left[K^{\text{sec}}\right]_{j=0}^{-1}\{\Delta S\}_i \tag{16}$$

Subsequently, the section deformation can be updated as in Eq. (17).

$$\{e\}_{j=1} = \{e\}_{j=0} + \{\Delta e\}_{j=1} \tag{17}$$

As section deformation vector $\{e\}_{j=1}$ is known at this stage, the fibre state determination process (in Sect. 2.4) can be carried out to compute the fibre resisting forces and fibre stiffness of all the fibres of the section. The section resisting force vector $\left\{S_{res}\right\}_{j=1}$ (see point G in Fig. 6) and the updated section stiffness $[K^{\text{sec}}]_{j=1}$ can be computed by assembling fibre resisting forces and stiffness for a given section deformation vector $\{e\}_{j=1}$. Then, the section unbalanced force vector $\left\{\Delta S_{\text{unb}}\right\}_{j=1}$ (see line GF' in Fig. 6) can be calculated as given in Eq. (18).

$$\left\{\Delta S_{\text{unb}}\right\}_{j=1} = \{S\}_i - \left\{S_{\text{res}}\right\}_{j=1} \tag{18}$$

If $\left\{\Delta S_{\text{unb}}\right\}_{j=1}$ is not within the prescribed tolerance, the algorithm will proceed into the next section-level iteration ($j = 2$) to compute a corrective section deformation increment $\{\Delta e\}_{j=2}$ based on $\left\{\Delta S_{\text{unb}}\right\}_{j=1}$ as given in Eq. (19).

$$\{\Delta e\}_{j=2} = [K^{\text{sec}}]_{j=1}^{-1}\left\{\Delta S_{\text{unb}}\right\}_{j=1} \tag{19}$$

This computation is schematically represented by line GG' in Fig. 6. Then, the section deformation vector $\{e\}_{j=2}$ is updated again by adding the corrective deformation $\{\Delta e\}_{j=2}$. Subsequently, fibre state determination (Sect. 2.4) is carried out on all the fibres in the section to compute the section resisting force vector $\left\{S_{res}\right\}_{j=2}$ (see point H in Fig. 6) and the section stiffness matrix $[K^{\text{sec}}]_{j=2}$ corresponding to the updated section deformation vector $\{e\}_{j=2}$, which can be utilized to calculate the unbalanced force $\left\{\Delta S_{\text{unb}}\right\}_{j=2}$ (see line HG' in Fig. 6). By continuing this process for several iterative steps, section unbalanced force $\left\{\Delta S_{\text{unb}}\right\}_j$ can be minimized to be under the tolerance prescribed in the formulation. In Fig. 6, the convergence has been achieved at the 3rd section-level iteration which corresponds to point H'.

It is important to note that minimization of $\left\{\Delta S_{\text{unb}}\right\}_j$ implies that the section force $\{S\}_i$ matches with the section resisting force $\left\{S_{\text{res}}\right\}_j$ which corresponds to the current section deformation $\{e\}_j$. This equilibrium state yields accurate section deformation and section stiffness for the given section force increment $\{\Delta S\}_i$.

Once section state determination is carried out on all the sections of a particular element, the updated section tangent stiffness matrices can be assembled to find the updated element tangent stiffness matrix $[K^e]_i$.

Fibre state determination

The fibre state determination process is designed to calculate the section resisting force vector $\left\{S_{\text{res}}\right\}_j$ and updated section stiffness matrix $[K^{\text{sec}}]_j$ corresponding to a given section deformation vector $\{e\}_j$ in the jth section-level iteration. The sections at control stations are divided into a sufficient number of uniaxial fibres as shown in Fig. 5. With the assumption that the plane section remains plane and perpendicular to the deformed longitudinal axis, axial strains of each fibre can be calculated using the given section deformation vector $\begin{Bmatrix} \varepsilon_0(x) \\ \boldsymbol{\Phi}(x) \end{Bmatrix}$ as given in Eq. (20)

$$\varepsilon_{\text{fib}} = \left\{1 \; -y_{\text{fib}}\right\}\begin{Bmatrix} \varepsilon_0(x) \\ \boldsymbol{\Phi}(x) \end{Bmatrix} \tag{20}$$

where $\varepsilon_0(x)$ represents axial strain at the centroid, $\boldsymbol{\Phi}(x)$ represents the curvature and y_{fib} denotes the distance to the fibre from the centroid. From the uniaxial material model assigned to each fibre, fibre stress σ_{fib} and fibre tangent stiffness $E_{\text{T,fib}}$ corresponding to fibre strain ε_{fib} can be obtained. Based on the fibre section model, section resisting forces can be calculated using Eq. (21) and the section stiffness can be calculated using Eq. (22) where A_{fib} denotes a fibre area.

$$\left\{S_{\text{res}}\right\}_j = \sum_{\text{nof}=1}^{\text{Nof}(x)} \begin{Bmatrix} 1 \\ -y \end{Bmatrix}\sigma_{\text{fib}}A_{\text{fib}} \tag{21}$$

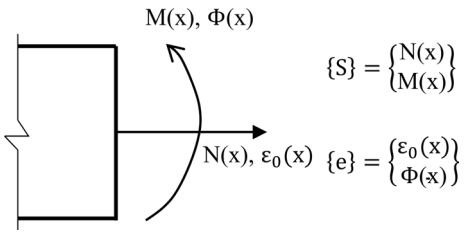

Fig. 7 Section forces and deformations at a control station

Author's personal copy

Table 1 Details of RW2 [35]

Height (mm)	3660
Outer perimeter depth × width (mm × mm)	1220 × 102
Aspect ratio (l/d)	3
Compressive axial load (kN)	240.41
Cube strength of concrete (MPa)	42.8
Yield strength of longitudinal reinforcement (MPa)	414
Concrete cracking strength (MPa)	$0.33\sqrt{f_c'}$

$$\left[K^{\text{sec}}\right]_j = \sum_{\text{nof}=1}^{\text{Nof}(x)} \begin{Bmatrix} 1 \\ -y \end{Bmatrix} E_{\text{T,fib}} A_{\text{fib}} \{1 - y\} \tag{22}$$

Experimental validation

The proposed model results were validated with experimental data of a cantilever wall RW2 [35] and a two-storey planar frame [36] by comparing the load–deformation responses. In addition, these specimens were also modelled using the OpenSees software [37] employing nonlinear fibre beam–column elements with same numerical parameters and material models. Furthermore, the internal axial stress and strain variations over the depth of each section in elements are discussed to describe the local behaviour of the models.

Cantilever wall

Table 1 gives the details of the wall RW2, and Fig. 8 illustrates the loading arrangement, the numerical model developed using OpenSees and proposed formulation and the reinforcement details of the cross section. It is important to note that the wall RW2 was designed for flexural dominant behaviour.

The numerical inputs and material models used in the proposed model and OpenSees software are tabulated in Table 2.

Figure 9a illustrates the load–deformation responses of the wall RW2 obtained by varying the number of integration points (nIP) along the element while all the sections are assigned same 20 no. of fibres. It can be noted in the figure

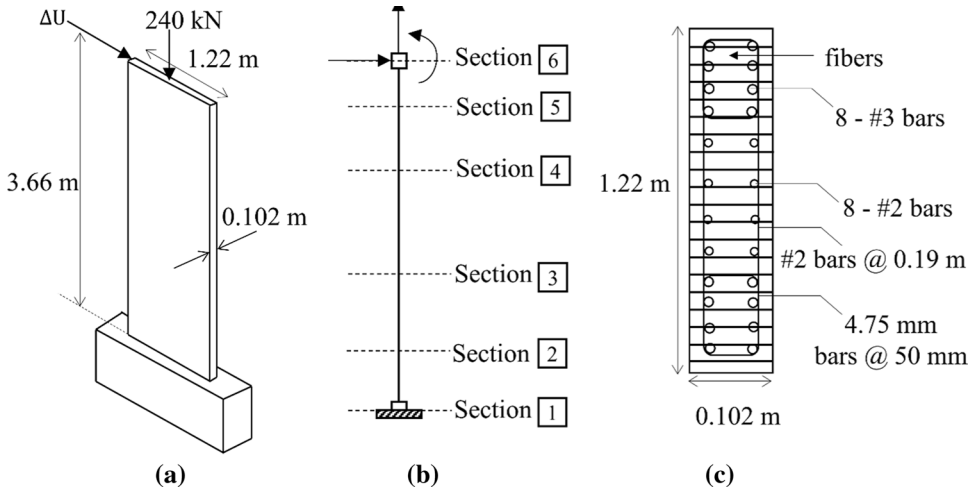

Fig. 8 Details of RW2 [35]; **a** loading arrangement and dimensions, **b** numerical model used for both OpenSees and proposed formulation analyses with integration point/section numbering and, **c** cross-sectional details with fibre discretization

Table 2 Numerical inputs and material models used in proposed model and OpenSees model of RW2

Input parameter	Novel formulation	OpenSees model
Number of elements	1	1
Number of integration points	6	6
Number of fibres	20	20
Section-level force tolerance norm	10^{-3}	–
Element-level residual deformation tolerance norm	–	10^{-8}
Structure-level force tolerance norm	10^{-5}	10^{-5}
Concrete compression model	Modified Kent and Park model	
Concrete post-cracking tension model	Linear tension softening model	
Steel material model	Bi-linear material model	

Author's personal copy

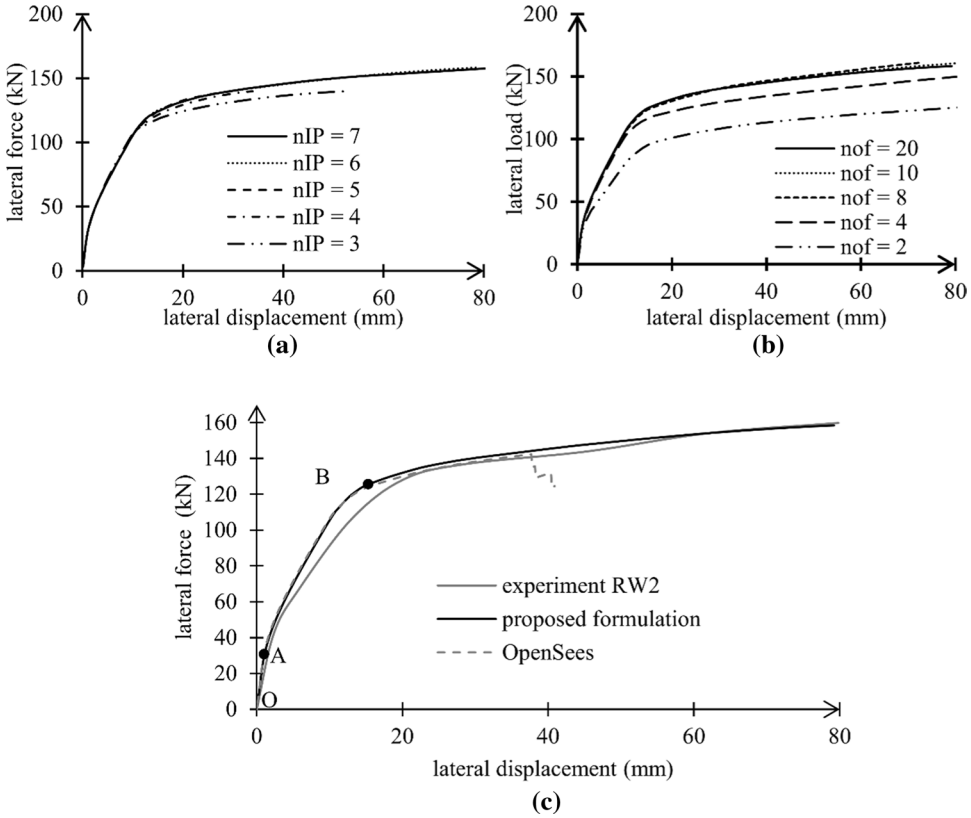

Fig. 9 Load deformation responses of the RW2 cantilever wall from the proposed formulation; **a** changing the number of integration points/sections (nIP), **b** changing the number of fibres (nof), **c** comparison with experimental and OpenSees response

that the results are converged beyond four no. of integration points. However, six integration points were assigned to each element for further analyses. Figure 9b illustrates the load–deformation responses of the wall RW2 obtained by varying the number of fibres (nIP) in a section while keeping six number of integration points assigned to the element constant. From the figure, it can be noted that the results are converged beyond 8 number of fibres assigned to the element. However, 20 fibres were assigned to each fibre section for further analyses. Figure 9c compares the load–deformation responses of the cantilever wall RW2, obtained using the proposed formulation, nonlinear force-based fibre beam–column element in OpenSees and the experiment.

The load–deformation responses in the three cases are in very good agreement. Around a lateral displacement of 40 mm, the OpenSees model fails to satisfy the compatibility relationship as element-level iteration fails to converge both element and section forces. This kind of numerical instability was not observed in the proposed formulation, where the convergence occurs at the section level by explicitly minimizing section unbalanced forces. This is further discussed in Sect. 4.2.

The local responses obtained from the proposed formulation accurately reflected the actual response of the cantilever wall reported in the experiment. The following section discusses the local response obtained from the proposed formulation at different load stages of the load–deformation response.

The sectional plots given in Figs. 10, 11, 12 and 13 illustrate the variation in axial strains and axial stresses at the six integration points or sections of the wall specimen RW2 for different load stages (see Fig. 8b). The axial strain variation across the depth at an integration point remains linear at all the load stages due to the assumption that plane section remains in plane and perpendicular to the deformed longitudinal axis. Up to the lateral load of 30 kN, the wall remains un-cracked and the load–deformation response behaves linear elastically. The sectional plots given in Fig. 10 illustrate the axial stress variations across the depths at all the integration points under the lateral load of 10 kN.

A significant reduction in the lateral stiffness of the wall was observed in the load–deformation curve beyond the lateral load of 30 kN (point A in load–deformation curve). This is mainly due to cracking of concrete fibres in the tensile zone near the support. The concrete fibres in compression zone and steel fibres in tension zone remain linear elastic. It should be further noted that some of the fibres in the tensile zone have already reached the concrete tensile strength and started to drop their tensile stresses significantly following the linear tension softening material model. Figure 11 illustrates the stress and strain distributions across the depths at all integration points at the lateral load of 63 kN. This load point

Author's personal copy

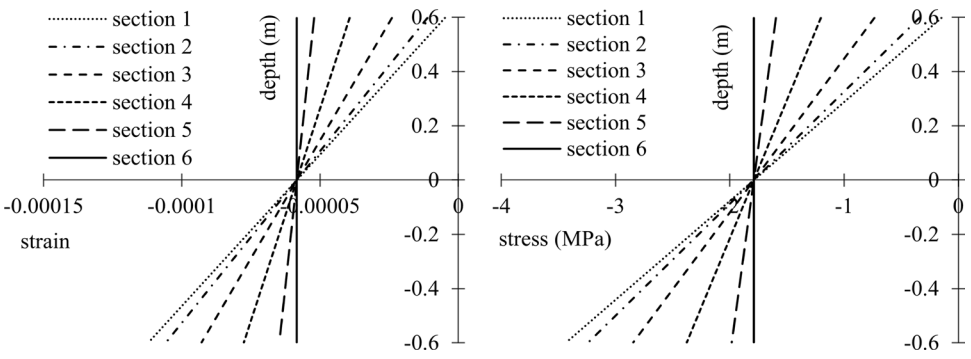

Fig. 10 Sectional plots at 10 kN load

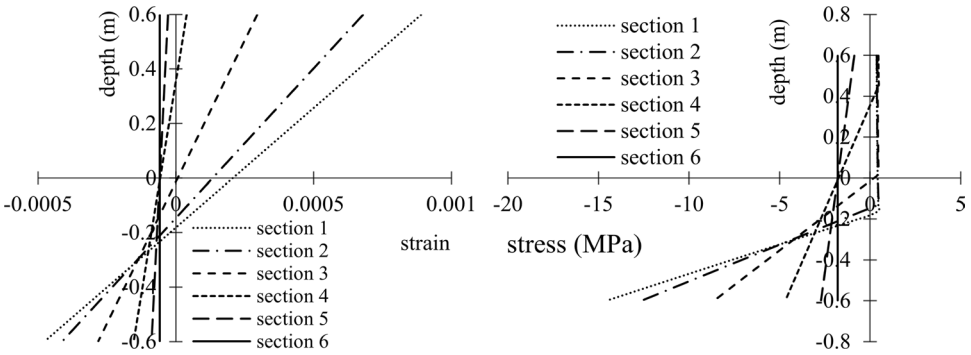

Fig. 11 Sectional plots at 63 kN load

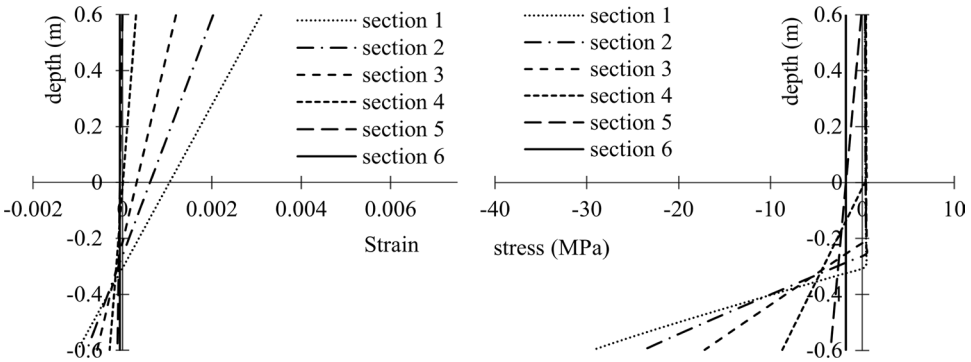

Fig. 12 Sectional plots at 115 kN load

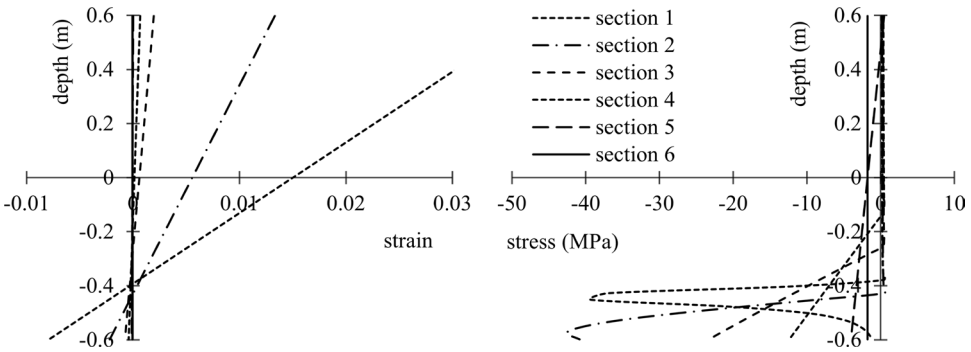

Fig. 13 Sectional plots at 154 kN load

represents the second branch (AB) of the load–deformation curve. It is also observed that the tensile zone gradually increases and the neutral axis is shifted towards the compression zone during the second branch AB. This can be observed by comparing the tension zones given in Figs. 11 and 12.

Author's personal copy

Beyond the lateral load of 125 kN (point B in load–deformation curve), the load–deformation response displays a ductile behaviour with a significant loss of stiffness, as a result of tensile reinforcement yielding near the support. Furthermore, a significant curvature concentration was observed at the integration point near the support (Sect. 1) as illustrated in Fig. 13. Due the excessive curvature concentration at the support (Sect. 1), some of the fibres in the compression zone have started reducing their compressive stresses resulting compression crushing. However, the reduction in compressive stresses of these fibres has not caused to reduce the section resisting moment which is sustained by the coupled forces in reinforcement bars.

Two-storey planar frame

Vecchio and Emara [36] have carried out an experimental study on a full-scale reinforced concrete frame to investigate the effect of shear mechanisms on the overall frame deformation, load carrying capacity and failure mode. The specimen tested was a one span, two-storey large-scale frame having a centre-to-centre span of 3.5 m and a storey height of 2 m. The frame was built integral with a large heavily reinforced base to simulate a fully fixed condition at the base. The concrete compressive strength at the test date was reported as 30 MPa. The frame columns were applied constant 700 kN axial loads, and the frame has been pushed from the top storey. The experimental set-up and reinforcement arrangements of the cross sections are given in Fig. 14. The steel material properties are given in Table 3. Numerical models were developed using the proposed formulation and OpenSees to predict the behaviour of the frame using numerical parameters given in Table 4.

Table 3 Reinforcement properties of frame [36]

Bar type	Area (mm^2)	f_y (MPa)	f_u (MPa)	E_s (GPa)
No. 20	300	418	596	192
No. 10	100	454	640	200

The predicted overall load–deformation response of the frame model developed by the proposed formulation is in a good agreement with the experimental results, as shown in Fig. 15. It is important to highlight that the proposed formulation does not account for geometrical nonlinearity; thus, the full ductility level of 150 mm lateral displacement was not predicted. However, the load capacity was well predicted along with the ductile behaviour to a lateral displacement around 65 mm.

The behaviour of the frame at different load levels reported in the experiment was well predicted by the proposed formulation. The flexural cracking was predicted at the ends of first storey beam around 65 kN, and a significant change in load–deformation response was observed. At around 135 kN, flexural cracking of the column bases was predicted; however, web cracks in the first storey beam were not predicted as the proposed element formulation neglects the shear deformation. The yielding of tensile reinforcement of the north and south end of the first storey beam was predicted around 230 kN and 235 kN, respectively. With further progression of load stages, hinging of the ends of first storey beam and yielding of both steel at column bases

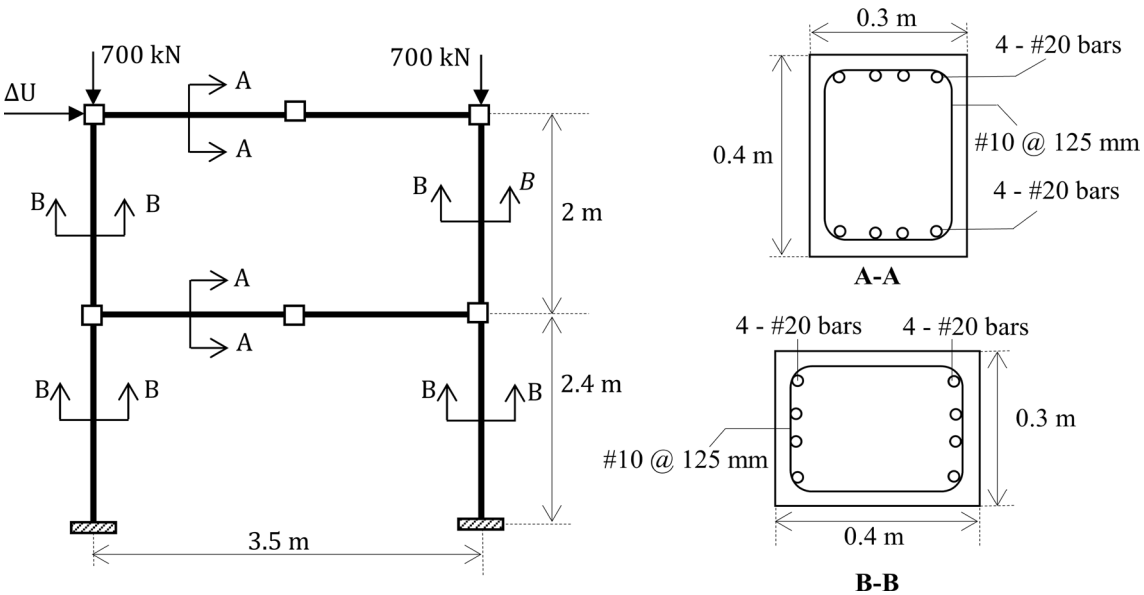

Fig. 14 Dimensions, mesh, loading arrangement and reinforcement details of all beams and columns of the planar reinforced concrete two-storey frame

Author's personal copy

Table 4 Numerical inputs used in proposed and OpenSees frame model

Input parameter	Novel formulation	OpenSees model
Number of elements (see Fig. 14)	8	8
Number of integration points	6	6
Number of fibres	40	40
Section-level force tolerance norm	10^{-3}	–
Element-level residual deformation tolerance norm	–	10^{-8}
Structure-level force tolerance norm	10^{-3}	10^{-3}
Concrete compression model	Modified Kent and Park model	
Concrete post-cracking tension model	Linear tension softening model	
Steel material model	Bi-linear material model	

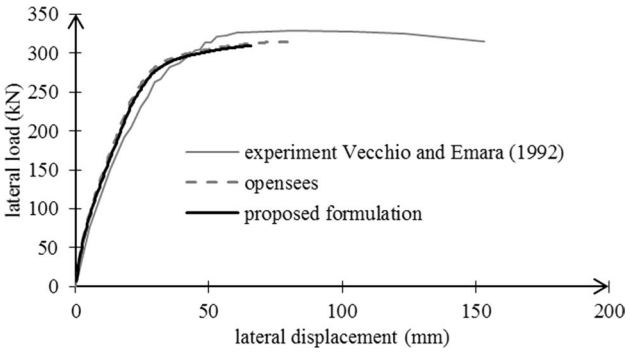

Fig. 15 Comparison of experimental load–deformation response of planar reinforced concrete two-storey frame using novel formulation and using OpenSees software

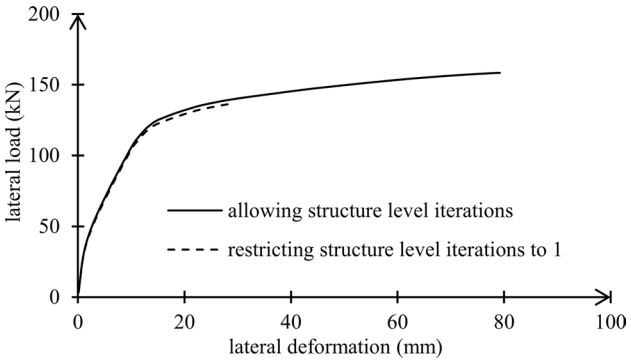

Fig. 16 Load deformation responses of RW2, allowing and restricting structure-level iterations using the proposed formulation

were observed at 285 kN. At 310 kN, concrete crushing and hinging were evident at the column bases while tensile steel at the top storey beam end too yielded.

Potential advantages of considering section-level equilibrium

Effective Newton–Raphson procedure at structure level

In the existing and proposed formulations, the structure-level iterative procedures are identical in terms of the computations carried out. In both cases, the structure unbalanced forces are minimized through the corrective load factors ($\Delta\lambda_i$) and corrective deformations ($\left\{ \begin{matrix} \Delta U_1 \\ \Delta U_2 \end{matrix} \right\}_{i=1}$) computed at each iteration, linearizing around the tangent stiffness matrix of the previous iteration. However, the two formulations differ from the method of computing structure resisting forces which are necessary to compute structure unbalanced forces. It should be noted that the speed of convergence depends on the method of computing structure resisting forces.

The existing formulation computes the structure resisting forces based on the element resisting forces which are converged to the estimated element nodal deformation. But in contrast, the proposed formulation computes the structure resisting force based on the updated tangent stiffness matrix converged to a given section force. It has been observed that the required number of structure-level iterations is lower when the resisting forces are calculated by converging to the section force. For example, suppose a structure is statically determinate and analysis is done using force control method. Here, the computed section force increments within the first structure-level iteration are exact for the applied load, irrespective of the stiffness assumed as the structure is statically determinate. In such a situation, the section state determination in first structure-level iteration yields the correct tangent stiffness for the applied force step as the section force increments calculated at the start.

In order to support this argument, the cantilever reinforced concrete wall, RW2, was analysed restricting Newton–Raphson iterations to one. Figure 16 provides a comparison of the load–deformation responses where a very good agreement could be seen. This reflects the effectiveness of

Author's personal copy

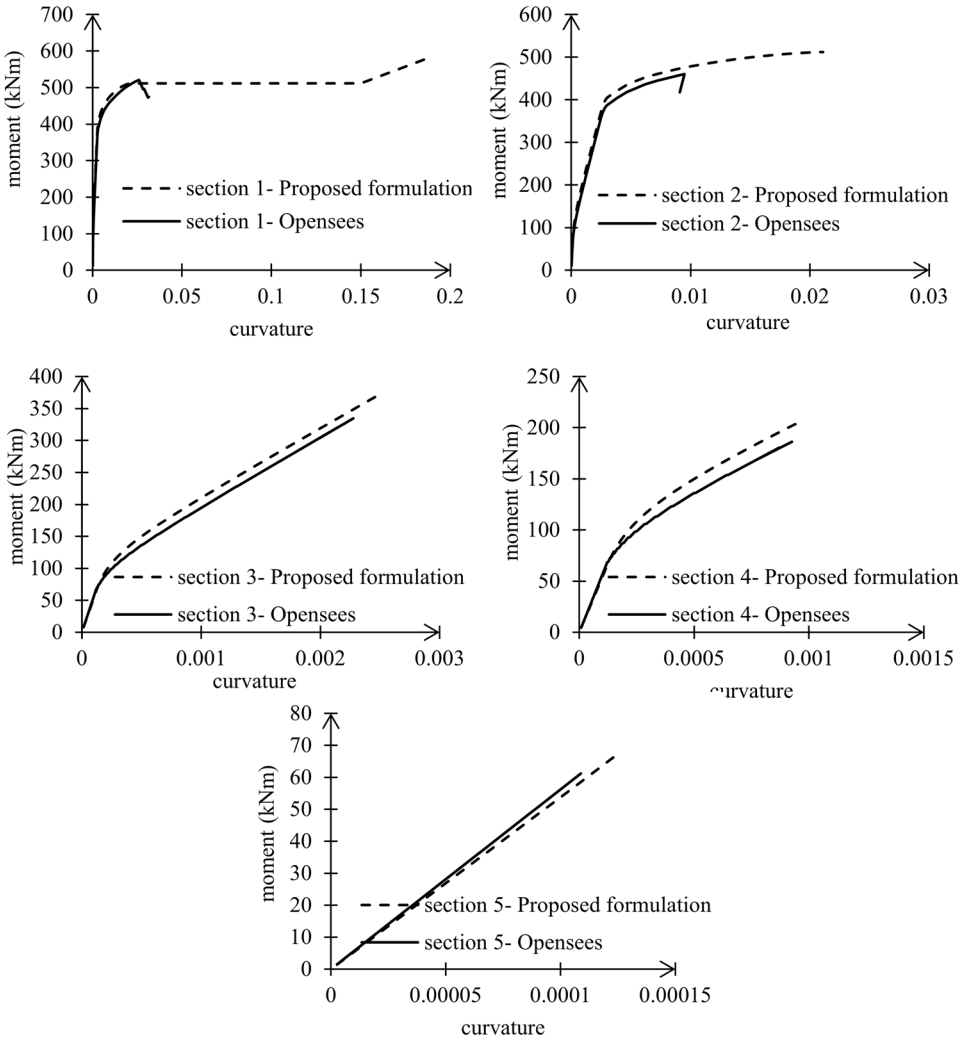

Fig. 17 Bending moment–curvature response of RW2 [35], using proposed formulation and Opensees

the Newton–Raphson process in the proposed formulation. Note that the analysis was done using displacement control method, and thus, the first structure-level iterations do not yield exact section forces.

Explicit satisfaction of section equilibrium

In the proposed formulation, the section-level iterative procedure computes an accurate section deformation and updated section tangent stiffness matrix for a given section force increment, by explicitly minimizing the section unbalanced forces. However, in the existing formulation, the element-level iterative procedure computes a series of element corrective forces to minimize element residual deformations while the sections follow these corrective forces to implicitly minimize section unbalanced forces. In this method, the agreement between the section force and section resisting force is not directly evaluated; thus, the element convergence cannot guarantee the minimization of section unbalanced forces in every situation. To support this argument, the moment–curvature relationships at integration points of the reinforced cantilever wall RW2 (see Fig. 8), obtained from the OpenSees software and the proposed formulation, were compared as shown in Fig. 17. They actually compare the moment–curvature responses when section equilibrium is implicitly and explicitly satisfied.

These plots demonstrate that in this particular example there is a difference in the moment curvature relationships in the two models, even though it does not affect the overall load–deformation response. It is important to highlight that the difference in sectional behaviour can be magnified and element convergence will be problematic in the existing formulation when cracked reinforced concrete constitutive relationships that can capture axial–flexure–shear interaction are implemented. The proposed formulation addresses this issue well by explicitly minimizing section unbalanced forces at section level itself maintaining section-level equilibrium throughout the analysis.

Author's personal copy

Conclusions

This paper presents a novel force-based finite element formulation to predict N–M interaction of RC frames and walls, considering section-level equilibrium. The proposed formulation employs two nested iterative procedures at structure level and section level where equilibrium is satisfied. The constitutive law is satisfied at fibre level while the law of compatibility is satisfied by the computation of correct section deformation and correct tangent stiffness for a given section force at the section level. The novel iterative procedure at the section level minimizes the section unbalanced forces at section level itself, preventing the generation of element residual deformations due to section unbalanced forces. This procedure allows to evaluate the agreement between section forces and section resisting forces directly, improving the accuracy of local behaviour which is important when implementing reinforced concrete crack models at the fibre level. The structure and element state determination processes were modified to accommodate the novel iterative procedure at the section level. The computation of element and structure resisting forces using updated tangent stiffness matrices increases the efficiency of structure-level iterative procedure. The proposed formulation was validated with a reinforced cantilever wall and a two-storey planar frame. The algorithm was proved to be accurate and numerically stable to predict N–M interaction of reinforced concrete frames and walls. Furthermore, it can be concluded that the proposed formulation enriches the existing force-based fibre beam–column element formulation, to capture section-specific phenomenon such as capturing the N–M–V interaction.

Compliance with ethical standards

Conflict of interest On behalf of all authors, the corresponding author states that there is no conflict of interest.

References

1. Krawinkler H (2006) Importance of good nonlinear analysis. Struct Des Tall Spec Build 15:515–531
2. Rajasankar J, Nagesh RI (2009) Modelling inelastic hinges using CDM for nonlinear analysis of reinforced concrete frame structures. Comput Concr 6(4):319–341
3. Ck IU (2016) Nonlinear analysis of the RC structures by higher-order element with the refined plastic hinge. Comput Concr 17(5):579–596
4. Tidemann L, Krenk SA (2018) Robust frame element with cyclic plasticity and local joint effects. Eng Struct 168:191–204
5. Colangelo F (2018) Effect of axial force-bending moment interaction of stochastic nonzero mean seismic response of reinforced concrete frames. Eng Struct 174:139–153
6. Nascimbene R (2015) Numerical model of a reinforced concrete building: earthquake analysis and experimental validation. Period Polytech Civ Eng 59(4):521–530
7. Casotto C, Silva V, Crowley H, Nascimbene R, Pinho R (2015) Seismic fragility of Italian RC precast industrial structures. Eng Struct 94:122–136
8. Brunesi E, Bolognini D, Nascimbene R (2015) Evaluation of the shear capacity of precast-prestressed hollow core slabs: numerical and experimental comparisons. Mater Struct 48:1503–1521
9. Azadi Kakavand MR, Neuner M, Schreter M (2018) A 3D continuum FE-model for predicting the nonlinear response and failure modes of RC frames in pushover analyses. Bull Earthq Eng 16:4893–4917
10. Markou G, Papadrakakis M (2013) Computationally efficient 3D finite element modeling of RC structures. Comput Concr 12(4):443–498
11. Terrenzi M, Spacone E, Camata G (2020) Comparison between phenomenological and fibre-section non-linear models. Front Built Environ 6:38
12. Guner S (2008) Performance assessment of shear-critical reinforced concrete plane frames. Ph.D. Dissertation, Department of Civil Engineering, University of Toronto, Toronto, ON, Canada
13. Li Z, Gao Y, Zhao Q (2016) A 3D flexure-shear fibre element for modeling the seismic behaviour of reinforced concrete columns. Eng Struct 117:372–383
14. Feng DC, Wu G, Sun ZY, Xu JG (2017) A flexure-shear Timoshenko fibre beam element based on softened damage-plasticity model. Eng Struct 140:483–497
15. Martinelli M (2008) Modeling shear-flexure interaction in reinforced concrete elements subjected to cyclic lateral loading. ACI Struct J 105(6):675–684
16. Spacone E, Filippou FC, Taucer FF (1996) Mixed formulation of nonlinear beam finite element. Comput Struct 58:71–83
17. Saritas A, Filippou FC (2013) Analysis of RC walls with a mixed formulation frame element. Comput Concr 12(4):519–536
18. Sharma C (2008) Displacement/mixed finite element formulation for beam and frame problems. M.sc Dissertation, European school of advanced studies in reduction of seismic risk ROSE school, Pavia, Italy
19. Correia AA, Almeida JP, Pinho R (2008) Force-based versus displacement-based formulations in the cyclic nonlinear analysis of RC frames. In: 14th World conference on earthquake engineering, Beiging, China
20. Menegotto M, Pinto PE (1973) Method of analysis for cyclically loaded reinforced concrete plane frames including changes in geometry and non-elastic behaviour of elements under combined normal force and bending. In: IABSE symposium on resistance and ultimate deformability of structures acted on by well-defined repeated loads, Lisbon, Portugal
21. Kaba S, Mahin SA (1984) Refined modeling of reinforced concrete columns for seismic analysis. In: EERC Report 84/03, Earthquake Engineering Research Center, University of California Berkeley, CA
22. Zeris CA, Mahin SA (1988) Analysis of reinforced concrete beam-columns under uniaxial excitation. J Struct Eng 114:804–820
23. Zeris CA, Mahin SA (1991) Behaviour of reinforced concrete structures subjected to biaxial excitation. J Struct Eng 117(9):2657–2673
24. Zeris CA (1986) Three dimensional nonlinear response of reinforced concrete buildings. Ph.D. Dissertation, Department of Civil Engineering, University of California Berkeley, CA
25. Ciampi V, Carlesimo L (1986) A nonlinear beam element for seismic analysis of structures. In: Proceedings of the 8th European conference on earthquake engineering, Lisbon, Portugal
26. Spacone E, Ciampi V, Filippou FC (1992) A beam element for seismic damage analysis. In: EERC report 92/08. Earthquake

Author's personal copy

Engineering Research Center, University of California, Berkeley, CA
27. Spacone E, Filippou FC, Taucer FF (1996) Fibre beam-column model for non-linear analysis of R/C frames: part I. Formulation. Earthq Eng Struct Dyn 25:711–725
28. Spacone E, Filippou FC, Taucer FF (1996) Fibre beam-column model for non-linear analysis of R/C frames: part II. Applications. Earthq Eng Struct Dyn 25:727–742
29. Monti G, Spacone E (2000) Reinforced concrete fibre beam element with bond slip. J Struct Eng 126(6):654–661
30. Lobo PS, Almeida J (2015) RC fibre beam-column model with bond-slip in the vicinity of interior joints. Eng Struct 96:78–87
31. Sabry S, Gendy FM, Ayoub A (2018) Displacement and mixed fibre beam elements for modelling of slender reinforced concrete structures under cyclic loads. Eng Struct 173:620–630
32. Souza RM (2000) Force-based Finite Element for Large Displacement Inelastic Analysis of Frames. Ph.D. Dissertation, University of California at Berkeley, CA
33. Coleman J, Spacone E (2001) Localization issue in force-based frame elements. J Struct Eng 127(11):1257–1265
34. Rajapakse RMCM, Wijesundara KK, Nascimbene R, Bandara CS, Dissanayake PBR (2019) Accounting axial-moment-shear interaction for force-based fibre modeling of RC frames. Eng Struct 184:15–36
35. Thomsen JH, Wallace JW (1995) Displacement-based design of reinforced concrete structural walls: an experimental investigation of walls with rectangular and T-shaped cross-sections. In: Report No. CU/CEE-95-06. Department of Civil and Environmental Engineering, Clarkson University, New York
36. Vecchio FJ, Emara MB (1992) Shear deformations in reinforced concrete Frames. ACI Struct J 89:46–56
37. McKenna F, Fenves GL, Scott MH (2000) Open system for earthquake engineering simulation. University of California, Berkeley

View publication stats